Process Modeling and Validation for Metal Big Area Additive Manufacturing

Srdjan Simunovic[1], Andrzej Nycz[1], Mark W. Noakes[1], Charlie Chin[2], and Victor Oancea[2]

[1]Oak Ridge National Laboratory, Oak Ridge, TN, USA

[2]Dassault Systemés SIMULIA Corporation, Johnston, RI, USA

Abstract: *Metal Big Area Additive Manufacturing (mBAAM) is a new additive manufacturing (AM) technology based on the metal arc welding. A continuously fed metal wire is melted by an electric arc that forms between the wire and the substrate, and deposited in the form of a bead of molten metal along the predetermined path. Objects are manufactured one layer at a time starting from the base plate. The final properties of the manufactured object are dependent on its geometry and the metal deposition path, in addition to depending on the basic welding process parameters. Computational modeling can be used to accelerate the development of the mBAAM technology as well as a design and optimization tool for the actual manufacturing process. We have developed a finite element method simulation framework for mBAAM using the new features of software ABAQUS. The computational simulation of material deposition with heat transfer is performed first, followed by the structural analysis based on the temperature history for predicting the final deformation and stress state. In this formulation, we assume that two physics phenomena are coupled in only one direction, i.e. the temperatures are driving the deformation and internal stresses, but their feedback on the temperatures is negligible. The experiment instrumentation (measurement types, sensor types, sensor locations, sensor placements, measurement intervals) and the measurements are presented. The temperatures and distortions from the simulations show good correlation with experimental measurements. Ongoing modeling work is also briefly discussed.*

1. Introduction

The distinguishing capability of metal Big Area Additive Manufacturing (mBAAM) is the ability to efficiently manufacture large, complex metal objects with medium near net shape accuracy. Compared to other metal Additive Manufacturing (AM) methods, the arc welding based AMs have lower capital cost, large build envelope, higher production rate, and well-established supply chains [1]. This type of AM technology has been actively pursued in recent years [1-3]. Computational modeling based on the Finite Element Method (FEM) have been used extensively in their process development [4]. They integrate thermal, mechanical, and metallurgical models, evolving geometry, material deposition, and disparate length and time scales. The various physics models are usually executed sequentially with the temperature history from thermal model used as the main driver for subsequent stress analysis and material models. The process involve multi-physics phenomena such as heat source interactions with the feedstock wire and the substrate [5-7], material properties at high temperatures [8, 9], heat transfer mechanisms [10], interactions between the deposited beads [11, 12], etc. The possibilities for in-situ experimental characterization [13] are limited due to bright arc, high temperatures and high electrical currents, so that it is necessary to calibrate the models on a controlled set of experiments and measurements.

In this paper, we present a development of thermo-mechanical computational models for mBAAM and their calibration against experiments. The developed simulations utilize a new, physics-based module for AM in the general-purpose software ABAQUS [16]. The models describe the macroscale heat transfer phenomena in the mBAAM process and the corresponding mechanical distortion and residual stress. In the next section, we describe the mBAAM equipment configuration and experiment setup. It is followed by the model formulations for materials, heat sources, and boundary conditions. The simulations of experiments are described next and compared to the experimental measurements. Ongoing work on the development of simulations and experimental validation on more complex build geometries is briefly described.

2. Experimental Setup

The mBAAM station made by Wolf Robotics, shown in Figure 1, is comprised of a protection work cell, ABB IRB 2600 robotic arm with IRC5 controller, Lincoln Electric R500 Power Wave welder, and a dual push-pull wire feeder. The manufacturing of a component is driven by its G-code command file which describes the sequence of wire deposition for building the component. The system adjusts to the substrate surface movement by modifying the vertical location of the welding torch. Between every interruption of wire deposition, the welding torch is automatically cleaned. The work cell is equipped with a 2D positioner which also serves as a print table for objects with a footprint of up to 0.8x0.8 meters. The build plate is mounted on the print table by toe clamps, and serves as the initial substrate for the printed parts.

In mBAAM, the welding torch, which is mounted on the end of the robotic arm, moves to the starting point of the bead deposition. The welding torch then starts laying down a molten bead of material along the path created by the slicer. When it reaches the end of the bead, it stops and travels to the beginning of the next bead. All beads deposited at the same vertical plane form a layer. The next layer beads are deposited on top of the previous layer/beads. The process continues until all the layers have been laid down.

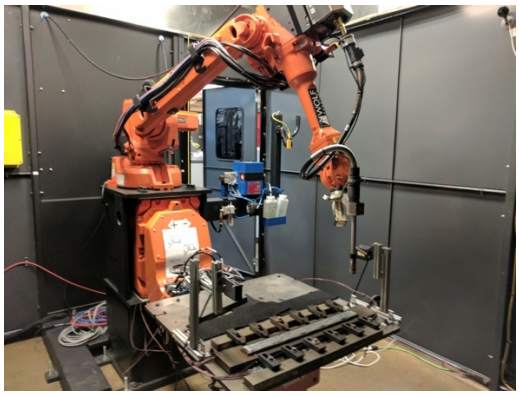

Figure 1: mBAAM equipment setup. The first manufactured object consists of four layers of deposited metal on a clamped build bar (center bottom of the image).

Three different experiments were conducted to support the development of the FEM simulation framework. The predominantly one-dimensional (1D) configuration (bar) and the two-dimensional (2D) configuration (wall) to investigate effects of various modeling approaches and process parameters. The calibrated models were then used to model the manufacturing of complex three-dimensional (3D) object (excavator boom). The 1D-type objects, named curl bars, were made by depositing four layers of material along the length of the build bar (Figure 1). Each layer consisted of a contour pass along the perimeter of the layer and a continuous fill-in of the layer. There was a total of eight traversals in the longitudinal direction (four continuous back and forth movements, with lateral offset). The 2D-type build object was a rectangular, thin wall build on a fully clamped build bar and was made of 124 layers of two continuous beads per layer. CAD models were created for all the printed objects, build plates, and the station table. They were exported as stereolithography (STL) files, sliced into layers, and converted into the motion and deposition commands (G-code) for the welding torch using customized in-house software.

In the partially clamped curl bar experiment, the build plate was mounted to the table using two non-symmetrically placed toe clamps (Figure 2a). The build plate was mounted this way to allow for measurement of unconstrained vertical displacement of the plate along the longitudinal direction. In the 2-D experiment (Figure 2b), the plate was held in place uniformly by an array of clamps.

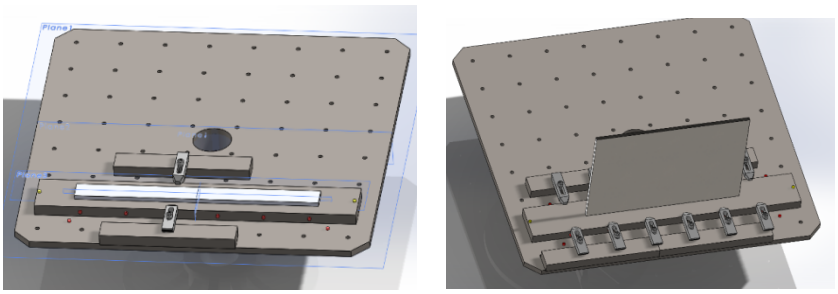

(a) (b)

Figure 2: Configurations of experiments: (a) partially clamped curl bar, (b) thin wall

A total of 20 thermocouples were used in each test. Six thermocouples were drilled into each side of the build plate. Additionally, three thermocouples were attached to the table on each side of the build plate. One thermocouple was installed on the bottom of the table, and one was installed in the center, below the surface of the table. The thermocouple locations are depicted in Figure 3a. Two laser range finders were mounted above the ends of the build plate (Figure 3a, b) to measure their displacement.

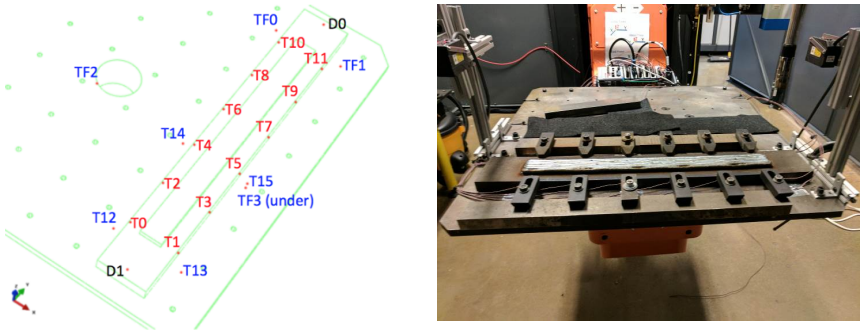

(a) (b)

Figure 3: Experiment instrumentation: (a) locations of the thermocouples in the build bar (T0-T11), thermocouples on the print table (T12-TF3), and range finders (D0, D1), (b) test configuration.

A National Instruments C-RIO 9035 embedded system was used to collect and synchronize data. It was equipped with digital, analog, and thermocouple dedicated interfaces. The digital inputs were used to acquire the status of the welding torch. The analog interfaces were used to read the displacement sensors and thermocouple inputs from the 20 thermocouples. A custom application was created to acquire, display, and save data. The data was collected at a frequency of 1Hz throughout the duration of the print. The print task time was variable and dependent on the part size and print conditions. Single data samples consisted of 20 temperatures, two displacements,

statuses of the deposition (on/off), and time stamps. The time stamping was necessary to synchronize the G-code information with the actual deposition sequence.

3. Methods

3.1 Physics-based Computational Framework

New, physics-based FEM formulations and models in ABAQUS 2017 [14] were used in this study. It is not the focus of this paper to describe these features in detail, but key aspects of the framework include:

Meshing: The geometric shape of the part whose 3D printing process is to be modeled is first discretized with finite elements. Arbitrary mesh densities can be used as generated by existing pre-processors. Using existing meshing technologies greatly improves and streamlines the analysis process. This is especially important because AM fabricated parts typically have very complex shapes that do not allow the use of uniform or layer-conforming meshes (difficult to generate).

Machine information: The 3D printing machine related information (e.g., powder recoating sequence, laser scan path, material deposition of the printing head, arc weld power, etc.) is pre-processed with no loss of accuracy from actual data as used by the physical machines. As far as the modeling process is concerned, no loss of accuracy is encountered by simplifying the information that the printing machine would use.

A new ABAQUS Intersection Module is used to sweep through the finite element mesh with the tool path and heat source configurations. The intersection can be based on either the original shape of the part or the current shape of the predicted deformed/distorted shape of the part during the analysis.

Progressive element activation: At any given point during the simulation, any finite element could be completely filled with mater, partially filled with matter, or completely empty. The software precisely keeps track of this evolution, keeps track of the mass inventory and distribution to account for the addition of the material during the printing

Progressive heating computations: at any point in time, heat bursts are computed by considering the actual path and power distribution of the heat source (the arc weld in this case). An arbitrary number of heating events (characterized as a sequence of heat fluxes at given locations) are computed for an accurate representation of the heating source in both time and space.

Progressive cooling via convection and radiation: partial facet areas are computed to allow for a very precise assessment of cooling related heat fluxes regardless of the finite element discretization. Radiation and convection cooling can be modeled on a continuously evolving surface that reflects the current shape of the part at any given point during the print.

Openness: a comprehensive set of new APIs are available to access information computed inside the code. While solutions for all major AM processes are provided, users can tailor physics modeling needs corresponding the particular process, machine environment, etc.

The usual heat transfer and stress divergence balance equations are leveraged and will not be reviewed here. Both a point-concentrated and a distributed volumetric heat flux model semi-

ellipsoid model heat source model [17] were considered. In the local *x*-*y*-*z* frame of the arc weld, where *x*-axis aligns with the arc weld moving direction, the laser heat source is described as

$$Q(x,y,z,t) = \frac{2P\eta}{\bar{a}\bar{b}\bar{c}\pi\sqrt{\pi}} \exp\left[-\left(\frac{(x+v_x t)^2}{\bar{a}^2} + \frac{(y)^2}{\bar{b}^2} + \frac{(z)^2}{\bar{c}^2}\right)\right] \quad (1)$$

Where P is the nominal power, η is the absorption coefficient, and v_x is the moving speed of the laser; t is the time; $\bar{a}$, $\bar{b}$, and $\bar{c}$ are the dimensions of the ellipsoid along *x*-, *y*-, and *z*-axes, respectively. The dimensions can be defined by the heat source parameters, including radius r, eccentricity e, and penetration depth d, as

$$\bar{a} = er, \ \ \bar{b} = \frac{r}{e}, \ \ \bar{c} = d \quad (2)$$

We have found that for mBAAM, the heat source parameters do not strongly influence the part scale temperature distribution. To speed up the calculations we approximated the heat source it in the following simulations by a point source.

Thermal radiation:

$$q_{rad} = \varepsilon\sigma((T - T_z)^4 - (T_\infty - T_z)^4) \quad (3)$$

and surface heat convection:

$$q_{conv} = h(T - T_\infty) \quad (4)$$

of free surfaces during manufacturing processes are considered, where ε is the material emissivity, h is convective coefficient, $\sigma = 5.67\times10^{-8}$ W/(m^2 · ℃^{4}) is the Stefan-Boltzmann constant, $T_z = -273.15$ ℃ is the absolute zero temperature, and T_∞ is the ambient temperature.

Temperature dependent material models for conductivity, specific heat, thermal expansion, elasticity and plasticity parameters were used as described below. A simple von Mises isotropic plasticity model was used for the mechanical response.

3.2 mBAAM Model Setup

The positioner table plate material is AISI 1020 steel. The build bars material was AISI 1018 steel. The test objects were printed with mild steel copper-coated welding wire from Lincoln Electric, ER70S-6 [15], of diameter 1.143mm. The chemical composition of the three steel materials is very similar so that their thermal properties were assumed to be identical. Thermal conductivity and heat capacity were derived based on carbon composition from reference [9], liquidus and solidus temperatures and latent heat were taken from reference [16]. Thermal conductivity as the function of temperature and the specific heat capacity were used from Heinze et al. [18] for ferrite/bainite/martensite. The coefficient of thermal expansion was taken from Figure and Table No 275R in Touloukian [17] . The temperature dependent mechanical properties for 1018 and 1020 steels were taken from Table 5 in Chen et al. [19]. The mechanical properties of the welding wire ER70S-6 were approximated by the properties of S355J2 steel [20], which has similar chemical composition. The measure ambient temperature was 22˚C. The constant value of convection film coefficient 0.018 mW/mm^2/˚C was used for the printed part, and values 0.015 or 0.02 mW/mm^2/˚C were used for the build plate. The heat source absorption coefficient was

assumed as 0.7. These values were approximated based on the range of values used in the literature [6, 21].

Model assemblies of the printed part, build plate, and the table plate were created based on each configuration as described in the experimental setup. In the model, the first layer of the printed part and the build plate share the same nodes. The objective was to make a preliminary evaluation of the new simulation methods and formulations for mBAAM so that the boundary conditions were simplified. Accordingly, the constant contact gap conductance of 0.5 $mW/mm^2/°C$ between the build plate and the table was applied in the region of the close thermal contact such as in the partially clamped region of the curl bar. The extent of this region depends on the build plate constraints, temperature and evolving deformation [6, 22], and was one of the calibration parameters in this study. No thermal Dirichelet boundary conditions were applied in the heat transfer analysis as none of the pieces in the experiment were thermostated. Therefore, convection and radiation occurs on all surfaces.

The positioner table and the build plate involved in the experiments act as significant heat sinks, so they were modeled to a reasonable detail. The overall dimensions of the positioner table are 812.8mm x 812.8mm x 15.875 mm and were modeled using hex elements. For the curl bar experiments, the build plate dimensions are 736.6mm x 101.6 x 25.4 mm and were modeled using hex elements. The printed part (558.8mm x 45mm x 10 mm) had to be modeled with higher resolution and the size of the hex elements was chosen to correspond with the deposited layer height of 2.5 mm. For the thin wall experiments, the build plate dimensions were 736.6mm x 101.6mm x 25.4 mm, and the printed part was 420mm x 9mm x 300 mm. Similar meshing considerations applied as above.

One of the key aspects of the new, physics-based framework in the software is that it does fully account for the actual tool path and energy information. The heat and material deposition account for all the pauses in the printing process associated with tool clean up and servicing. Two speed/power settings were used in most cases. Nominal power and deposition speeds were used. For the first layer, the deposition speed was 4.2 mm/sec, and the power was 2720 Watts. For subsequent layers, the speed was 6.8 mm/sec, and the power was 2430 Watts. The welding wire is fed with constant speed of 84.7 mm/s. The high intensity heat source follows the experimentally recorded tool path, heats, melts, and fuses the consumable and substrate materials. The highly transient heat transfer balance is performed and temperature evolution is calculated as the build progresses. These temperature distribution history (time and space) is used in a stress analysis static analysis to evaluate stresses and distortions.

4. Computational Simulations

4.1 Partially Clamped Curl Bar

To compare the simulation with experimental results, we extracted from the model time histories of temperature at 12 locations (T0-T11 in Figure 3a) and the displacement histories at locations D0 and D1. Figures 4-6 show the temperature comparisons between the experiments (all in red, labelled *_test) and the simulations for two convection coefficients, h=0.02 and 0.015 $mW/mm^2/°C$. Even with these simple choices of constant convection coefficients, the curves

compare reasonably well (although, there is certainly room for improvement). At the left section of build plate at T0 and T1 in Figure 3(a) and (b), the simulation using h=0.015 (in green) match well with the test data (in red); whereas at T2 and T3 in Figure 3(c) and (d), the simulation using h=0.02 (in blue) (i.e. more convection and hence more cooling) matches better with the test data.

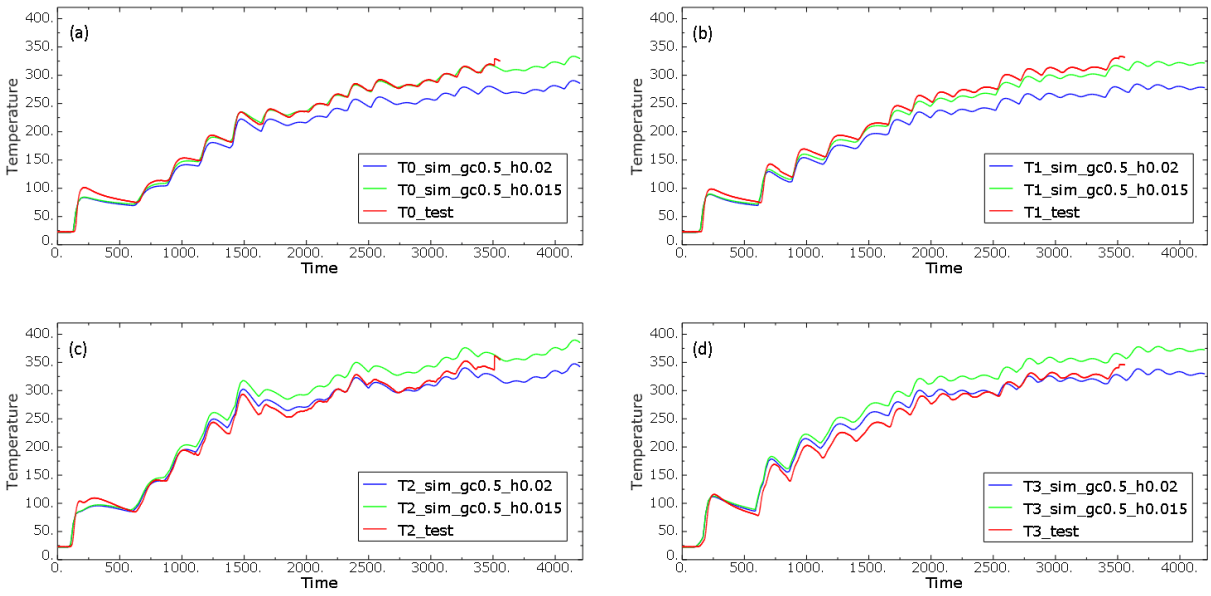

Figure 4: Temperature history comparison between the test and simulation results at thermocouple (a) T0, (b) T1, (c) T2, and (d) T3 on the build plate.

In the middle section of build plate, thermocouples T4 and T5 near the clamps and at T6 and T7 in Figure 5, the simulation using h=0.02 mW/mm^2/°C matches data slightly better.

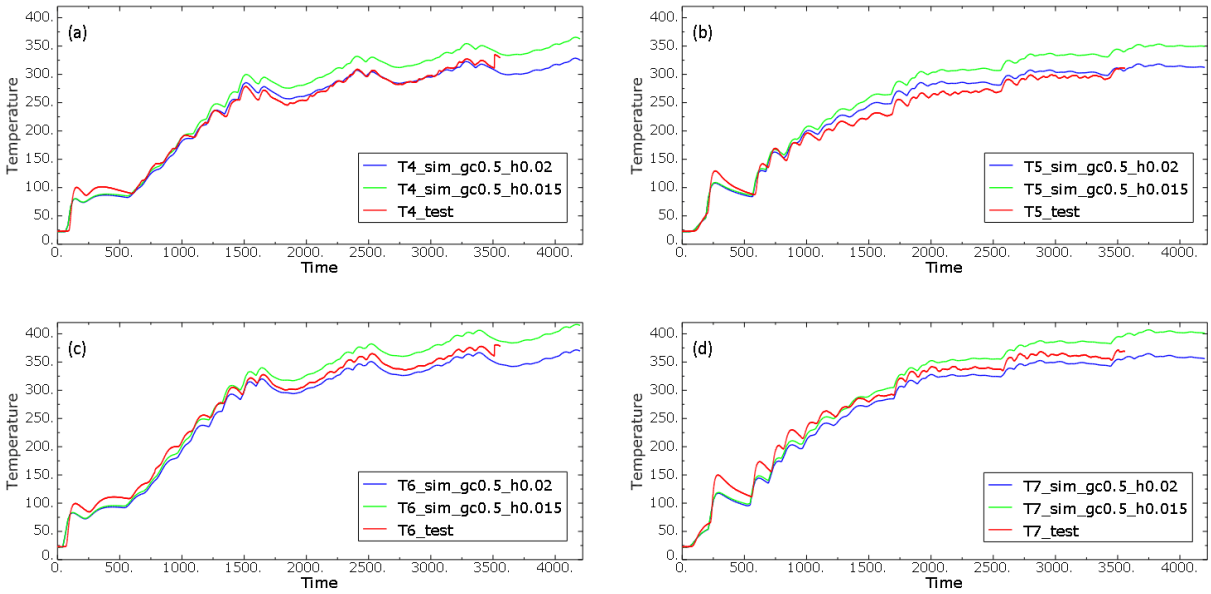

Figure 5: Temperature history comparison between the test and simulation results at thermocouple (a) T4, (b) T5, (c) T6, and (d) T7 on the build plate.

Temperatures at T8-T11 locations on the right section of the build plate are shown in Figure 6. The simulations using h=0.015 mW/mm^2/°C result in slightly lower temperatures than the test data. A better match can be obtained by decreasing the convection coefficient for less cooling in this section. The use of space-dependent convection coefficients would also account for the effect of welding blankets placed around the build bar to protect the wires for thermocouples.

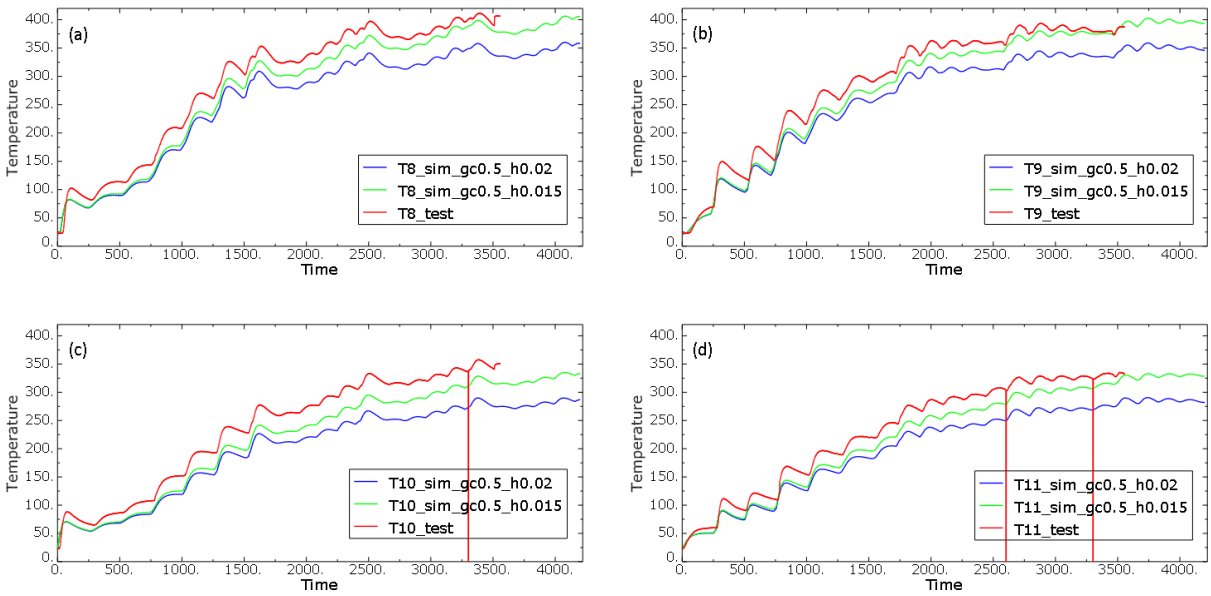

Figure 6: Temperature history comparison between the test and simulation results at thermocouple (a) T8, (b) T9, (c) T10, and (d) T11 on the build plate.

Despite a minimal calibration effort, the temperatures correlate reasonably well with either choice of convection coefficients. A contour plot on the temperature field shortly after the printing has ended is shown in Figure 7a.

The temperature histories from heat analysis were mapped (space and time) into subsequent structural analysis. The part undergoes overall upward bending distortion as illustrated by the experimental curves in Figure 8a and 8b. The molten material is added at the top of the printed part, and after a brief thermal expansion period, it contracts as it cools down, and causes shortening. The final computed configuration of the build plate onto which the upward displacements are measured is shown in Figure 7b.

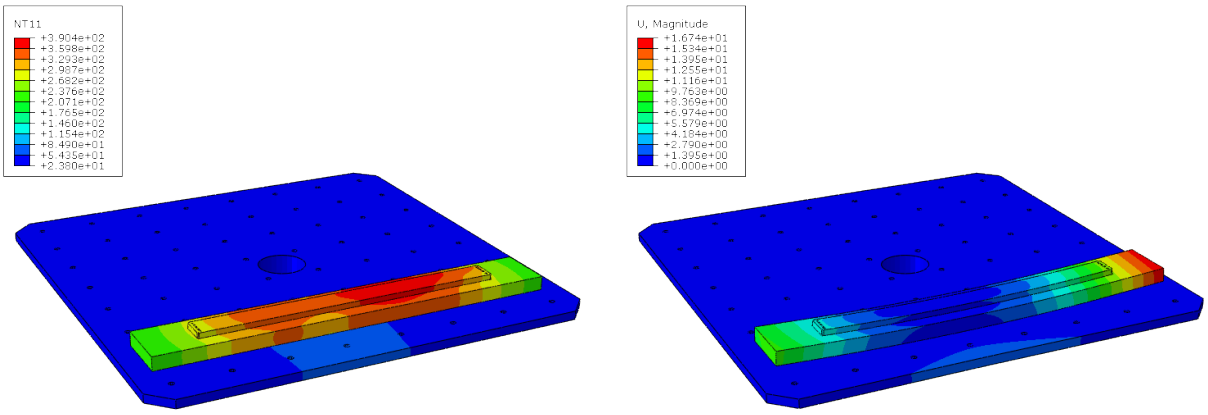

(a) (b)

Figure 7: (a) Temperature shortly after printing (°C); (b) Displacements (mm)

The measured displacement at D0 and D1 on the build plate are compared to the simulation (Figure 8a). There were no modifications to any of the material parameters including the coefficients of thermal expansion. The deformation trends are captured, although there is room for improvement. Some of the uncertainty and oscillations in the experimental data originate from the flexibility of the measurement setup.

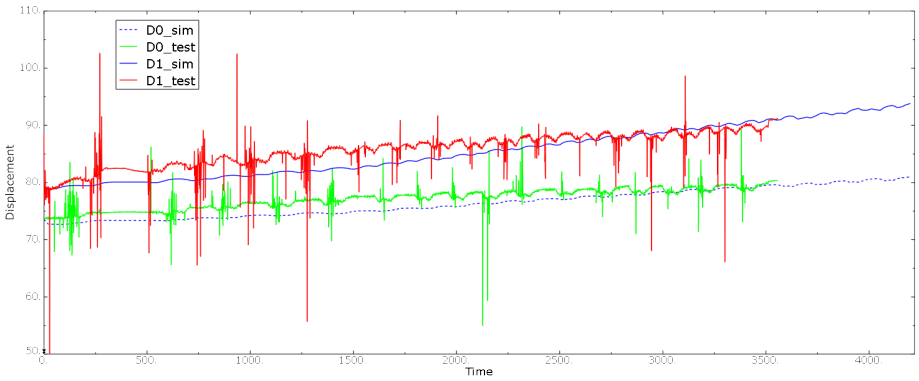

(a)

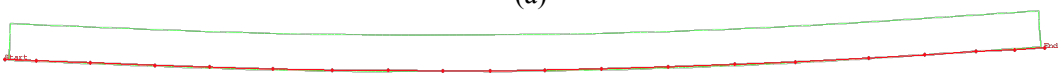

(b)

Figure 8: a) Displacement histories comparison between the test and simulation results at D0 and D1 on the build plate; b) Final deformed configuration (red - experimental bottom surface, vs green – simulation result for the build plate)

In Figure 8b, the final deformation profile of the simulated curlbar (green) is plotted against the experimentally measured profile of the bottom surface (red).

4.2 Thin Wall

Figure 9a shows temperature contour plots at various stages during the more than five-hour print. A rather coarse time increment of 55 seconds for a total of 344 increments was used. As in any transient FEM analysis, the reported solution (in this case temperatures) reflect all sources for heating and cooling during increments. In the early stages, there is more conduction into the massive build plate and positioning table which is reflected in lower temperatures. As the print builds up, the intensity of the heat conduction from the heat source into the build plate and table is reduced, so that the overall temperature increases.

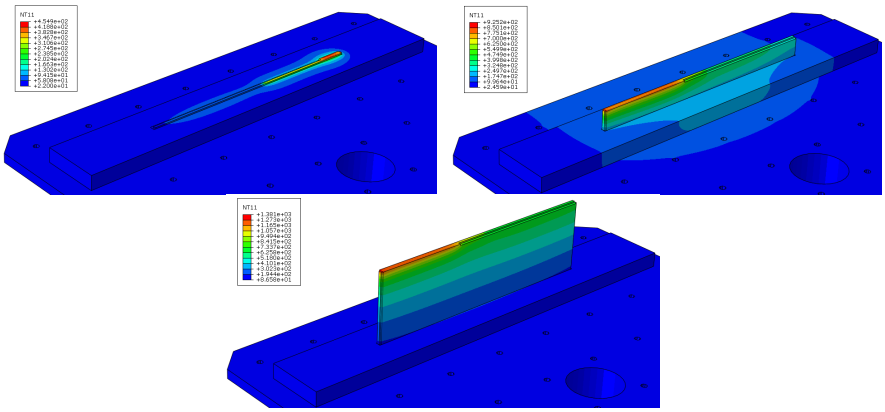

(a)

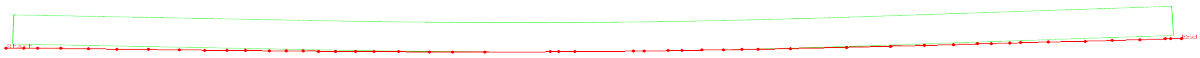

(b)

Figure 9.a) Thin wall thermal contour plots at various stages during printing; b) Final deformed configuration (red - experimental bottom surface vs. green – simulation result for the build plate).

In Figure 9b, the final deformation profile of the simulated curlbar (in green) after the numerical clamps was removed is plotted against the experimentally measured profile of the bottom surface. As it can be observed, the agreement is very good.

Using the constant film coefficients, h=0.02 and h=0.018 mW/mm^2/°C, for the printed part and the build bar, respectively, the simulated temperatures (Figure 10, green curves) again match very well the experimental thermocouple data (red curves) for the first hour of simulated printing. Afterwards, the simulations exhibit slower cooling rates when compared to the experiment. This

departure is associated with increasing effect of the radiative heat transfer as the wall grows. Using the temperature dependent combined heat transfer model (blue curves), developed for a similar AM process [6], significantly improves the correlation with the experiment.

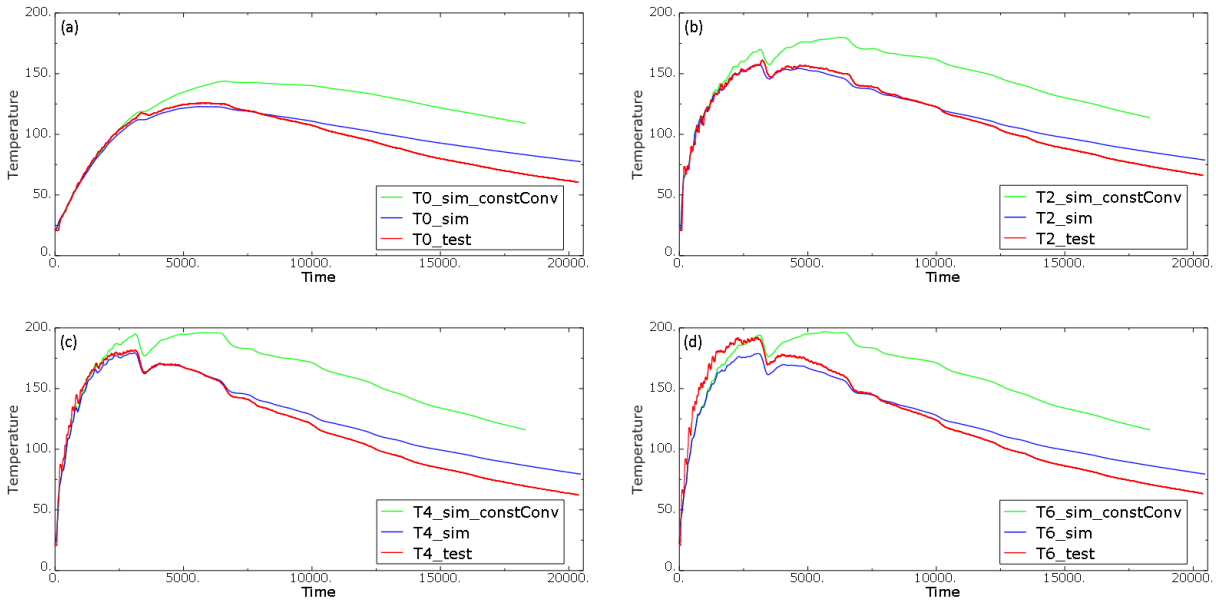

Figure 10: Temperature history comparison between the test and simulation results at thermocouple (a) T0, (b) T2, (c) T4, and (d) T6 on the build plate.

4.3 Excavator Arm

The final goal of the ongoing computation analysis is to assess the accuracy and efficiency of the simulation tools for predicting temperature, distortion, and residual stress evolutions in large parts. In Figure 11a shows a photograph of the two-meter high part of interest, and Figure 11b shows the corresponding FEM model.

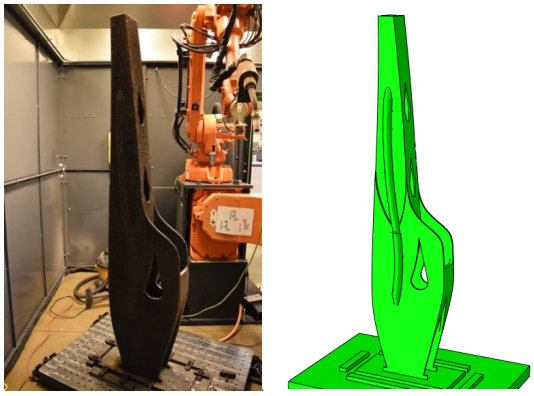

Figure 11: (a) Left: Photo of the printed excavator arm; (b) Numerical model.

It takes approximately 70 hours to print this object so there is a clear incentive to replace experimentation with simulations as much as possible. Figure 12 shows simulated temperatures at various stages during the print. Simulations can be used to assess the final distortions and the residual stresses in the printed part, and investigate efficiency of various printing strategies.

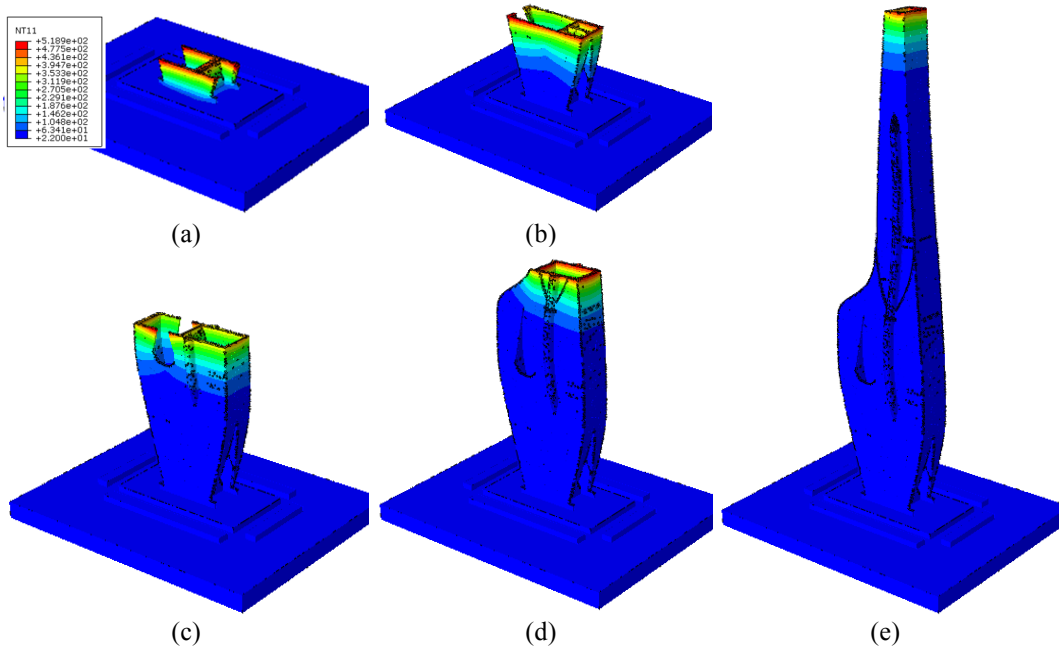

Figure 12: Preliminary results for temperature contour plots at several stages during print.

5. Conclusions

We have presented a preliminary development of simulations for Metal Big Area Additive Manufacturing (mBAAM) using FEM program ABAQUS/Standard. The supporting experiments range from small (0.01 m high) to large (2m high). The small parts were used to develop the best simulation practices and to calibrate the process and boundary condition models. The simulation of large excavator arm demonstrates the feasibility of computational modeling for simulating practical mBAAM manufacturing problems. Numerical modeling, as in many other applications, can be a cost-effective tool in gaining insight into the formidable multi-scale/multiphysics challenges that AM process in general pose. Our initial results show that with minimal calibration efforts a good correlation with the physical experiments was achieved. Much remains to be explored. Ongoing work includes improving calibration for the heat transfer models, models for distortion predictions, residual stresses, and material microstructure.

6. Acknowledgements

Research was sponsored by the U.S. Department of Energy, Office of Energy Efficiency and Renewable Energy, Advanced Manufacturing Office, under contract DE- AC05-00OR22725 with UT-Battelle, LLC.

7. References

[1] D. H. Ding *et al.*, "Towards an automated robotic arc-welding-based additive manufacturing system from CAD to finished part," *Computer-Aided Design,* vol. 73, pp. 66-75, Apr 2016.

[2] D. H. Ding, Z. X. Pan, D. Cuiuri, and H. J. Li, "Wire-feed additive manufacturing of metal components: technologies, developments and future interests," *International Journal of Advanced Manufacturing Technology,* vol. 81, no. 1-4, pp. 465-481, Oct 2015.

[3] P. M. Dickens, M. S. Pridham, R. C. Cobb, I. Gibson, and G. Dixon, "Rapid prototyping using 3-D welding," in *The Seventh Annual Solid Freeform Fabrication Symposium*, Austin, TX, 1992.

[4] J. Ding *et al.*, "Thermo-mechanical analysis of Wire and Arc Additive Layer Manufacturing process on large multi-layer parts," *Computational Materials Science,* vol. 50, no. 12, pp. 3315-3322, Dec 2011.

[5] N. Yadaiah and S. Bag, "Effect of Heat Source Parameters in Thermal and Mechanical Analysis of Linear GTA Welding Process," *ISIJ International,* vol. 52, no. 11, pp. 2069-2075, 2012.

[6] X. W. Bai, H. O. Zhang, and G. L. Wang, "Improving prediction accuracy of thermal analysis for weld-based additive manufacturing by calibrating input parameters using IR imaging," *International Journal of Advanced Manufacturing Technology,* vol. 69, no. 5-8, pp. 1087-1095, Nov 2013.

[7] A. S. Azar, S. K. As, and O. M. Akselsen, "Determination of welding heat source

parameters from actual bead shape," *Computational Materials Science,* vol. 54, pp. 176-182, Mar 2012.

[8] F. Cverna, *Thermal Properties of Metals, ASM ready reference*. Materials Park, OH: ASM International, 2002.

[9] S. Yafei, T. Yongjun, S. Jing, and N. Dongjie, "Effect of Temperature and Composition on Thermal Properties of Carbon Steel," *Ccdc 2009: 21st Chinese Control and Decision Conference, Vols 1-6, Proceedings,* pp. 3756-3760, 2009.

[10] M. Abid and M. Siddique, "Numerical simulation to study the effect of tack welds and root gap on welding deformations and residual stresses of a pipe-flange joint," *International Journal of Pressure Vessels and Piping,* vol. 82, no. 11, pp. 860-871, Nov 2005.

[11] J. Xiong, G. J. Zhang, H. M. Gao, and L. Wu, "Modeling of bead section profile and overlapping beads with experimental validation for robotic GMAW-based rapid manufacturing," *Robotics and Computer-Integrated Manufacturing,* vol. 29, no. 2, pp. 417-423, Apr 2013.

[12] D. H. Ding, Z. X. Pan, D. Cuiuri, and H. J. Li, "A multi-bead overlapping model for robotic wire and arc additive manufacturing (WAAM)," *Robotics and Computer-Integrated Manufacturing,* vol. 31, pp. 101-110, Feb 2015.

[13] J. A. Goldak and M. Akhlaghi, *Computational Welding Mechanics*. Springer, 2005.

[14] "ABAQUS Analysis User's Manual," Dassault Systemes Simulia Corp.2017.

[15] T. L. E. Company, "Lincoln ER70S-6," T. L. E. Company, Ed., ed. Cleveland, OH, 2016, pp. 1-2.

[16] J. W. H. Price, A. Ziara-Paradowska, S. Joshi, T. Finlayson, C. Semetay, and H. Nied, "Comparison of experimental and theoretical residual stresses in welds: The issue of gauge volume," *International Journal of Mechanical Sciences,* vol. 50, no. 3, pp. 513-521, Mar 2008.

[17] Y. S. Touloukian, R. K. Kirby, R. E. Taylor, and P. D. Desai, *Thermal Expansion, Metallic Elements and Alloys* (Thermophysical Properties Of Matter). IPI/Plenum, 1975.

[18] C. Heinze, A. Pittner, M. Rethmeier, and S. S. Babu, "Dependency of martensite start temperature on prior austenite grain size and its influence on welding-induced residual stresses," *Computational Materials Science,* vol. 69, pp. 251-260, Mar 2013.

[19] J. Chen, B. Young, and B. Uy, "Behavior of high strength structural steel at elevated temperatures," *Journal of Structural Engineering-Asce,* vol. 132, no. 12, pp. 1948-1954, Dec 2006.

[20] J. Outinen and P. Makelainen, "Mechanical properties of structural steel at elevated temperatures and after cooling down," *Fire and Materials,* vol. 28, no. 2-4, pp. 237-251, Mar-Aug 2004.

[21] N. Pepe, S. Egerland, P. A. Colegrove, D. Yapp, A. Leonhartsberger, and A. Scotti, "Measuring the process efficiency of controlled gas metal arc welding processes," *Science and Technology of Welding and Joining,* vol. 16, no. 5, pp. 412-417, Jul 2011.

[22] M. P. Mughal, H. Fawad, and R. Mufti, "Finite element prediction of thermal stresses and deformations in layered manufacturing of metallic parts," *Acta Mechanica,* vol. 183, no. 1-2, pp. 61-79, May 2006.